



**Calhoun: The NPS Institutional Archive**  
**DSpace Repository**

---

Theses and Dissertations

1. Thesis and Dissertation Collection, all items

---

1994-09

A transmission electron microscope  
characterization of sodium sulfate hot  
corrosion of silicon carbide fiber-reinforced  
lithium aluminosilicate glass-ceramic matrix composite

Hunt, Richard K.

Monterey, California. Naval Postgraduate School

---

<http://hdl.handle.net/10945/30944>

---

This publication is a work of the U.S. Government as defined in Title 17, United States Code, Section 101. Copyright protection is not available for this work in the United States.

*Downloaded from NPS Archive: Calhoun*



Calhoun is the Naval Postgraduate School's public access digital repository for research materials and institutional publications created by the NPS community. Calhoun is named for Professor of Mathematics Guy K. Calhoun, NPS's first appointed -- and published -- scholarly author.

**Dudley Knox Library / Naval Postgraduate School**  
**411 Dyer Road / 1 University Circle**  
**Monterey, California USA 93943**

<http://www.nps.edu/library>

# NAVAL POSTGRADUATE SCHOOL

## Monterey, California



## THESIS

A TRANSMISSION ELECTRON MICROSCOPE  
CHARACTERIZATION OF SODIUM SULFATE  
HOT CORROSION OF SILICON CARBIDE  
FIBER-REINFORCED LITHIUM  
ALUMINOSILICATE  
GLASS-CERAMIC MATRIX COMPOSITE

by

Richard K. Hunt

September 1994

Thesis Advisor:

Alan G. Fox

Approved for public release; distribution is unlimited

Thesis  
RD4726

DUDLEY KNOX LIBRARY  
NAVAL POSTGRADUATE SCHOOL  
MONTEREY CA 93943-5101

# REPORT DOCUMENTATION PAGE

Form Approved  
OMB No. 0704-0188

Public reporting burden for this collection of information is estimated to average 1 hour per response, including the time for reviewing instructions, searching existing data sources, gathering and maintaining the data needed, and completing and reviewing the collection of information. Send comments regarding this burden estimate or any other aspect of this collection of information, including suggestions for reducing this burden, to Washington Headquarters Services, Directorate for Information Operations and Reports, 1215 Jefferson Davis Highway, Suite 1204, Arlington, VA 22202-4302, and to the Office of Management and Budget, Paperwork Reduction Project (0704-0188), Washington, DC 20503.

1. AGENCY USE ONLY (Leave blank)		2. REPORT DATE September 1994		3. REPORT TYPE AND DATES COVERED Master's Thesis	
4. TITLE AND SUBTITLE A Transmission Electron Microscope Characterization of Sodium Sulfate Hot Corrosion of Silicon Carbide Fiber-Reinforced Lithium Aluminosilicate Glass-Ceramic Matrix Composite				5. FUNDING NUMBERS	
6. AUTHOR(S) Hunt, Richard K.					
7. PERFORMING ORGANIZATION NAME(S) AND ADDRESS(ES) Naval Postgraduate School Monterey CA 93943-5000				8. PERFORMING ORGANIZATION REPORT NUMBER	
9. SPONSORING / MONITORING AGENCY NAME(S) AND ADDRESS(ES) Naval Air Warfare Center Warminster PA 18974				10. SPONSORING / MONITORING AGENCY REPORT NUMBER	
11. SUPPLEMENTARY NOTES The views expressed in this thesis are those of the author and do not reflect the official policy or position of the Department of Defense or the U.S. Government.					
12a. DISTRIBUTION / AVAILABILITY STATEMENT Approved for public release; distribution is unlimited.				12b. DISTRIBUTION CODE A	
13. ABSTRACT (Maximum 200 words) Sodium Sulfate hot corrosion of a SiC/LAS composite was studied using conventional transmission electron microscopy and selected area diffraction. Changes in the morphology, composition and crystallography of the phases in the glass-ceramic matrix and the fiber/matrix interface were studied. Microchemical analysis using energy dispersive x-ray spectroscopy (EDS) was also performed on all phases detected. Three samples were studied: (1) as-received, (2) no salt coating and annealed in argon, and (3) sodium sulfate coated and annealed in oxygen. Both heat treatments were performed at 900 C for 100 hours. Sample (1) matrix was composed of small stoichiometric grains of Beta-spodumene ( $\text{Li}_2\text{O} \cdot \text{Al}_2\text{O}_3 \cdot 4\text{SiO}_2$ ) and mullite ( $3\text{Al}_2\text{O}_3 \cdot 2\text{SiO}_2$ ) in a high silica glass (88 wt% $\text{SiO}_2$ and 12 wt% $\text{Al}_2\text{O}_3$ ). The fiber/matrix interface consisted of an amorphous $\text{SiO}_2$ and graphitic carbon layer. Sample (2) showed a substantial decrease in mullite content with a concomitant increase in the alumina content of the glass and crystalline phases. The interface morphology appeared unchanged by annealing in argon. Sample (3) suffered considerable hot corrosion. The matrix was a very fine mixture of glass and Beta-spodumene polycrystallites (20 nm in diameter). The fiber/matrix interface was extensively corroded and formed an alternating layered structure of graphitic carbon and amorphous $\text{SiO}_2$ .					
14. SUBJECT TERMS Lithium Aluminosilicate, SiC Fiber-Reinforced Composites				15. NUMBER OF PAGES 86	
				16. PRICE CODE	
17. SECURITY CLASSIFICATION OF REPORT Unclassified		18. SECURITY CLASSIFICATION OF THIS PAGE Unclassified		19. SECURITY CLASSIFICATION OF ABSTRACT Unclassified	
				20. LIMITATION OF ABSTRACT UL	



Approved for public release; distribution is unlimited.

A Transmission Electron Microscope Characterization of  
Sodium Sulfate Hot Corrosion of Silicon Carbide Fiber-Reinforced Lithium  
Aluminosilicate Glass-Ceramic Matrix Composite

by

Richard K. Hunt  
Lieutenant, United States Coast Guard  
B.S., United States Coast Guard Academy, New London, CT, 1986


Submitted in partial fulfillment  
of the requirements for the degree of

MASTER OF SCIENCE IN MECHANICAL ENGINEERING


from the


NAVAL POSTGRADUATE SCHOOL  
September 1994

Author:

  
Richard K. Hunt

Approved by:

  
Alan G. Fox, Thesis Advisor

  
Matthew D. Kelleher, Chairman  
Department of Mechanical Engineering

## ABSTRACT

Sodium Sulfate hot corrosion of a SiC/LAS composite was studied using conventional transmission electron microscopy and selected area diffraction. Changes in the morphology, composition and crystallography of the phases in the glass-ceramic matrix and the fiber/matrix interface were studied. Microchemical analysis using energy dispersive x-ray spectroscopy (EDS) was also performed on all phases detected. Three samples were studied: (1) as-received, (2) no salt coating and annealed in argon, and (3) sodium sulfate coated and annealed in oxygen. Both heat treatments were performed at 900 C for 100 hours.

Sample (1) matrix was comprised of small stoichiometric grains of  $\beta$ -spodumene ( $\text{Li}_2\text{O}-\text{Al}_2\text{O}_3-4\text{SiO}_2$ ) and mullite ( $3\text{Al}_2\text{O}_3-2\text{SiO}_2$ ) in a high silica glass (88 wt%  $\text{SiO}_2$  and 12 wt%  $\text{Al}_2\text{O}_3$ ). The fiber/matrix interface consisted of an amorphous  $\text{SiO}_2$  and graphitic carbon layer. Sample (2) showed a substantial decrease in mullite content with a concomitant increase in alumina content of the glass and crystalline phases. The interface morphology appeared unchanged by annealing in argon. Sample (3) suffered considerable hot corrosion. The matrix was a very fine mixture of glass and  $\beta$ -spodumene polycrystallites (20 nm in diameter). The fiber/matrix interface was extensively corroded and formed an alternating layered structure of graphitic carbon and amorphous  $\text{SiO}_2$ .

*TRC 13*  
*H94726*  
*C.2*

## TABLE OF CONTENTS

I.	INTRODUCTION . . . . .	1
II.	BACKGROUND . . . . .	3
	A. SiC FIBER-REINFORCED LAS COMPOSITES. . . . .	3
	B. FIBER/MATRIX INTERFACES . . . . .	12
	C. CORROSION OF SiC/LAS COMPOSITES BY $\text{Na}_2\text{SO}_4$ . . . . .	14
	D. SEM AND XRD ANALYSIS OF SiC/LAS COMPOSITES . . . . .	21
III.	SCOPE OF PRESENT WORK . . . . .	23
IV.	EXPERIMENTAL PROCEDURE . . . . .	26
	A. THIN FOIL SAMPLE PREPARATION . . . . .	27
	B. TRANSMISSION ELECTRON MICROSCOPY. . . . .	28
V.	RESULTS AND DISCUSSION. . . . .	30
	A. AS-RECEIVED . . . . .	30
	B. NO SALT COATING, HEAT-TREATED IN ARGON . . . . .	42
	C. SALT COATED, HEAT-TREATED IN OXYGEN . . . . .	46
VI.	CONCLUSIONS . . . . .	56
VII.	RECOMMENDATIONS . . . . .	58
VIII.	APPENDIX A: SEM MICROGRAPHS AND X-RAY DIFFRACTOGRAMS . . . . .	60

IX. APPENDIX B: CORRODED INTERFACE EDS SPECTRA . . . . 63

LIST OF REFERENCES . . . . . 72

INITIAL DISTRIBUTION LIST . . . . . 75

## LIST OF FIGURES

Figure 1.	The lithium-aluminosilicate system ternary phase diagram . . . . .	5
Figure 2.	The lithium-aluminosilicate system pseudo-binary phase diagram . . . . .	5
Figure 3.	Longitudinal thermal expansion of solid solutions of $\beta$ -spodumene ( $\text{Li}_2\text{O}-\text{Al}_2\text{O}_3-\text{nSiO}_2$ ). . . . .	6
Figure 4.	Volume expansion of $\beta$ -spodumene . . . . .	7
Figure 5.	Longitudinal thermal expansion of $\beta$ -eucryptite in $a_0$ and $c_0$ directions and for polycrystalline structures . . . . .	8
Figure 6.	Flexural strength (3-point) of LAS-SiC yarn composites . . . . .	10
Figure 7.	Fracture toughness, $K_{IC}$ of LAS-SiC yarn composites . . . . .	10
Figure 8.	Crack impeding process in fiber-reinforced matrix . . . . .	11
Figure 9.	Schematic of gas turbine engine showing proposed structural applications for ceramics . . . . .	15
Figure 10.	Types of corrosive attack as a function of reciprocal temperature . . . . .	16
Figure 11.	Schematic of $\text{SiO}_2$ protective oxide scale on SiC fiber . . . . .	17
Figure 12.	Plot of Carbon, Silicon, and Oxygen composition over a Nicalon fiber cross-section . . . . .	19
Figure 13.	Stress-strain curves of LAS-SiC tensile specimens exposed to varying atmospheres . . . . .	20
Figure 14.	Schematic comparison of the electron beam excitation volume for SEM and TEM . . . . .	23

Figure 15.	Optical micrograph of 3 mm diameter disc after thinning to approximately 50 $\mu\text{m}$ showing the fiber orientation within the matrix . . . . .	28
Figure 16.	TEM bright field micrograph of the as-received thin foil sample with crystalline phases, glassy matrix, inclusions and a fiber/matrix interface. . . . .	30
Figure 17.	EDS spectra for mullite phase in the as-received sample . . . . .	31
Figure 18.	EDS spectra for $\beta$ -spodumene phase in the as-received sample . . . . .	32
Figure 19.	(a) TEM micrograph of mullite phase, (b) mullite [310] zone axis pattern . . . . .	33
Figure 20.	TEM micrograph of $\beta$ -spodumene phase . . . . .	34
Figure 21.	Elongated $\text{ZrO}_2$ particles in glassy matrix in as-received sample . . . . .	35
Figure 22.	$\text{ZrO}_2$ [110] Zone Axis Pattern . . . . .	35
Figure 23.	Bright field image of fiber/matrix interface in as-received sample . . . . .	36
Figure 24.	Dark field image of fiber/matrix interface in as-received sample, using the 002 graphite reflection . . . . .	38
Figure 25.	Selected area diffraction pattern from the interface and glassy matrix in as-received sample . . . . .	39
Figure 26.	Selected area diffraction pattern from the Nicalon fiber in as-received sample . . . . .	40
Figure 27.	(a) Bright field image of Nicalon fiber, (b) dark field image of Nicalon fiber in the as-received sample, using 111 $\beta$ -SiC reflection . . . . .	41
Figure 28.	Comparison of x-ray diffractograms from the as-received and heat treated in argon samples showing decrease in mullite content . . . . .	43

Figure 29.	Comparison of x-ray diffractograms from (a) as-received sample, and (b) the annealed in argon sample showing the presence of $\beta$ -eucryptite . . . . .	44
Figure 30.	EDS spectrum for $\beta$ -eucryptite phase in the heat treated in argon sample . . . . .	45
Figure 31.	Bright field TEM micrograph of the sodium sulfate coated and annealed in oxygen sample . . . . .	46
Figure 32.	(a) Amorphous matrix prior to being irradiated with condensed electron beam, (b) SADP ring pattern from the matrix corresponding to $\beta$ -spodumene crystallites .	47
Figure 33.	(a) Recrystallized matrix after being irradiated with condensed electron beam, (b) SADP ring pattern from recrystallized matrix . . . . .	49
Figure 34.	Binary $\text{Al}_2\text{O}_3$ - $\text{SiO}_2$ phase diagram . . . . .	50
Figure 35.	Bright field TEM micrograph of a corroded fiber/matrix interface used for EDS analysis . . . . .	51
Figure 36.	Bright field TEM micrograph of a corroded fiber/matrix interface . . . . .	53
Figure 37.	Dark field TEM micrograph of the corroded fiber/matrix interface from Figure 35, using the 002 graphite reflection . . . . .	54
Figure 38	SEM backscattered electron micrographs of (a) as-received, (b) noncoated and annealed in argon, and (c) $\text{Na}_2\text{SO}_4$ coated and annealed in oxygen samples [Ref. 17] . . . . .	61
Figure 39	X-ray diffractograms of (a) as-received, (b) noncoated and annealed in argon, and (c) $\text{Na}_2\text{SO}_4$ coated and annealed in oxygen samples [Ref. 17] . . . . .	62
Figure 40.	EDS spectrum corresponding to position 1 on the corroded fiber/matrix interface shown in Figure 35 . . . . .	64
Figure 41.	EDS spectrum corresponding to position 2 on the corroded fiber/matrix interface shown in Figure 35 . . . . .	65



<b>Figure 42.</b>	EDS spectrum corresponding to position 3 on the corroded fiber/matrix interface shown in Figure 35 . . . . .	. 66
<b>Figure 43.</b>	EDS spectrum corresponding to position 4 on the corroded fiber/matrix interface shown in Figure 35 . . . . .	. 67
<b>Figure 44.</b>	EDS spectrum corresponding to position 5 on the corroded fiber/matrix interface shown in Figure 35 . . . . .	. 68
<b>Figure 45.</b>	EDS spectrum corresponding to position 6 on the corroded fiber/matrix interface shown in Figure 35 . . . . .	. 69
<b>Figure 46.</b>	EDS spectrum corresponding to position 7 on the corroded fiber/matrix interface shown in Figure 35 . . . . .	. 70
<b>Figure 47.</b>	EDS spectrum corresponding to position 8 on the corroded fiber/matrix interface shown in Figure 35 . . . . .	. 71

## ACKNOWLEDGMENTS

I would like to convey my sincere appreciation to Professor Alan G. Fox for his expert instruction on the TEM, guidance as thesis advisor, and assistance in helping me complete this thesis. The results of this work are directly reflective of the outstanding quality of his tutelage. I would also like to thank Dr. Shaio-Wen Wang from the Naval Air Warfare Center for providing me with the opportunity to study a very interesting and "on the cutting edge of technology" topic. Lastly, I would like to thank my wife, Rondi and daughter, Rachel for their unconditional support and love during my work at Naval Postgraduate School, without you none of this would have been possible.

## I. INTRODUCTION

The U. S. Navy is considering silicon carbide fiber-reinforced lithium aluminosilicate (SiC/LAS) glass-ceramic matrix composites as a replacement for nickel based superalloys currently used in gas turbine engine components. Attempts to improve gas turbine power and efficiency involves increasing the turbine operating temperature ( $T_{T4}$ ) beyond that sustainable by the nickel superalloys. SiC/LAS composites offer the advantages of being lightweight, which leads to lower overall engine weight and reduced stress on rotating components; the composites also possess very low (or even negative) coefficients of thermal expansion, high strength, improved toughness, high melting temperature, and good resistance to corrosion at elevated temperatures.

The operating environment of the marine gas turbine engine is usually hostile, in that the atmosphere is often humid and salty. All grades of fuel contain some amount of sulfur which may combine with airborne contaminants to form sodium sulfate deposits and accumulate on engine components. These deposits have been found to be responsible in part for the degradation of the SiC/LAS composite mechanical properties.

There has been a great deal of research on the hot corrosion of silicon based ceramic monoliths such as SiC and  $\text{Si}_3\text{N}_4$ . However, very little work has been done concerning

the hot corrosion of a SiC/LAS composite. Further studies in this area are required to fully understand the driving forces and kinetics of the corrosion process in the composite to ensure proper utilization in future applications.

Previous work has been performed at the Naval Postgraduate School and the Naval Air Warfare Center, Warminster, Pennsylvania to characterize the phases present in a composite subjected to hot corrosion by sodium sulfate. These analyses were accomplished with the scanning electron microscope equipped with an energy dispersive x-ray spectrometer and an x-ray diffractometer.

The focus of the present study is to conduct a thin foil transmission electron microscope analysis of the samples previously studied in the SEM. The lower limit of spatial resolution of the TEM will enable very accurate EDS data and chemical composition to be collected for each phase present, and coupled with zone axis diffraction patterns and the previously obtained x-ray diffraction data, the phase and microstructures present within the matrix and the interface chemistry and morphology can be positively identified.

## II. BACKGROUND

### A. SiC FIBER-REINFORCED LAS GLASS-CERAMIC COMPOSITES

A glass-ceramic is a fine grained crystalline ceramic material which is formed as a base glass and then devitrified. The type of crystalline phases formed depends primarily on initial composition, thermal treatments, and the nucleating agents employed. The mechanical properties of glass ceramics are influenced by the volume fraction of the crystalline and non-crystalline phases, crystal size and distribution, and the crystal-to-glass interfacial bond strength [Ref. 1]. Typically, the crystalline phase is the dominant constituent present (70-100 vol.%), thus its physical and chemical properties have the greatest influence on the overall glass-ceramic properties. The crystalline phase usually has much greater strength, which can be attributed to its very small grain size and uniform microstructure. The fine grain size is achieved by the addition of nucleating agents such as  $ZrO_2$  and  $TiO_2$  into the glass prior to devitrification. As the percentage of nucleating agents increases, the grain size has been found to decrease [Ref. 2].

Although glass-ceramics exhibit very high strength, they are brittle at room temperature and do not exhibit the ductility and plasticity usually common to metals. Glass-ceramics behave elastically up to the fracture strain. This

brittle behavior has been attributed to restricted dislocation motion resulting from large Burgers vectors, the presence of few slip systems, and the strong ionic bonding which must be broken during slip [Ref. 3]. Because of the elastic behavior, any crack which develops is not hindered by plastic deformation ahead of the crack tip, allowing it to propagate rapidly leading to brittle failure.

The lithium aluminosilicate ( $\text{Li}_2\text{O}-\text{Al}_2\text{O}_3-\text{SiO}_2$ ) system has been studied extensively and is widely used in cookware and appliances and base substrates for computer chips due to its very low (or even negative) coefficient of thermal expansion. Glass-ceramic materials based on the LAS system are primarily substances where the main crystalline phase may be a metastable solid solution of  $\beta$ -quartz (transparent) or a stable solid solution of  $\beta$ -spodumene or  $\beta$ -eucryptite (opaque). The important crystalline phases in the LAS system are eucryptite ( $\text{Li}_2\text{O}-\text{Al}_2\text{O}_3-2\text{SiO}_2$ ), spodumene ( $\text{Li}_2\text{O}-\text{Al}_2\text{O}_3-4\text{SiO}_2$ ), and petalite ( $\text{Li}_2\text{O}-\text{Al}_2\text{O}_3-8\text{SiO}_2$ ); these lie on the connecting line in the ternary diagram (Figure 1) within the glass forming region. The low temperature  $\alpha$ -eucryptite and  $\alpha$ -spodumene are transformed upon heating into stable solid solutions of  $\beta$ -eucryptite and  $\beta$ -spodumene at roughly 972 C and 500 C respectively, as seen in Figure 2. The structure of  $\beta$ -eucryptite ( $\text{LiAlSiO}_4$ ) is derived from the hexagonal form of  $\beta$ -quartz and similarly the structure of  $\beta$ -spodumene is derived from the tetragonal form of  $\text{SiO}_2$ .

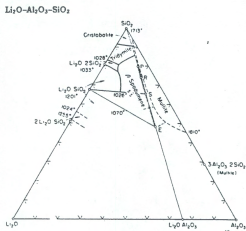
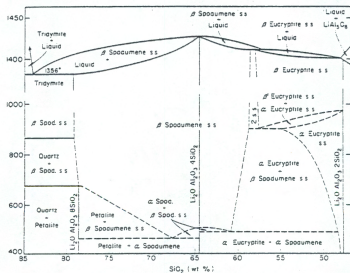


Figure 1. LAS Ternary Phase Diagram. [Ref. 4].



**Figure 2.** LAS Binary Phase Diagram. P=petalite, E=eucryptite, Q=quartz, S=spodumene, s.s.=solid solution, L=liquid [Ref. 4].



Opaque glass-ceramics are commonly manufactured so that the primary crystalline phase is  $\beta$ -spodumene. This is because of its very low (or even negative) coefficient of thermal expansion (CTE). This property is easily tailored to meet specific applications by controlling the chemical composition and the crystallization conditions. The  $\beta$ -eucryptite crystalline phase also offers the advantages of a very low CTE, and is similarly controllable. In tetragonal  $\beta$ -spodumene, the low CTE's are attributed to a strong longitudinal anisotropy [Ref. 5]. Under the influence of increasing temperature, the crystal tends to expand in the  $c_0$  direction and contracts along the  $a_0$  axis, with a net result of a very low volumetric expansion. A graph showing the longitudinal thermal expansion of  $\beta$ -spodumene is shown in Figure 3.

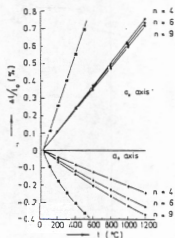


Figure 3. Longitudinal thermal expansion of solid solutions of  $\beta$ -spodumene ( $\text{Li}_2\text{O}-\text{Al}_2\text{O}_3-n\text{SiO}_2$ ) [Ref. 5].

The volume expansion of  $\beta$ -spodumene is also dependent on the  $\text{SiO}_2$  content in the separated solid solutions, and is shown in Figure 4.

Similarly,  $\beta$ -eucryptite tends to expand along the  $a_0$  axis and contract in the  $c_0$  direction with increasing temperature, again resulting in a very low overall CTE. This dependence is shown in Figure 5.

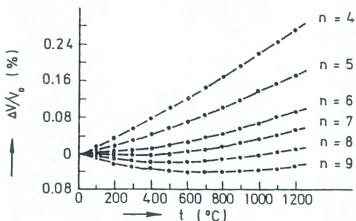


Figure 4. Volume expansion of  $\beta$ -spodumene ( $\text{Li}_2\text{O}-\text{Al}_2\text{O}_3-\text{nSiO}_2$ ) [Ref. 5].

In addition to low CTE's, LAS glass-ceramics also possess many other favorable properties such as a high elastic modulus (for ceramic materials), high melting point, and good resistance to oxidation at elevated temperatures.

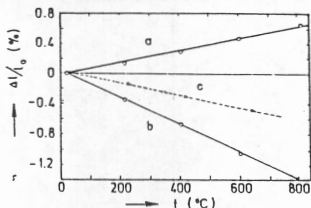


Figure 5. Longitudinal thermal expansion of  $\beta$ -eucryptite in (a)  $a_0$  direction, (b)  $c_0$  direction, and (c) polycrystalline structure [Ref. 5].

Silicon Carbide (SiC) fiber reinforced LAS glass-ceramic matrix composites are excellent candidates for use as a structural material in high temperature applications. The composite material has excellent strength, improved toughness, high melting temperature, and resistance to oxidation at high temperatures. The most attractive property of the composite is its improved toughness, which approaches that of some metals.

The LAS matrix is a prime candidate for use in this composite because (1) since it is a glassy matrix, the composite can be easily fabricated without fiber damage due to the viscous flow of the matrix at elevated temperatures associated with the hot-pressing process, (2) the thermal treatment causes the glass to recrystallize into stable solid

solutions, and (3) its physical and chemical thermal stability is generally better than organic or metallic matrix materials [Ref. 6]. The LAS elastic modulus is roughly 60 to 100 GPa, which coupled with that of the reinforcing fibers by volume fraction ( $E_c = V_f E_f + V_m E_m$ ) produces good composite strength through load transfer from matrix to the fiber. Figures 6 and 7 clearly demonstrate the improved strength and fracture toughness of the SiC/LAS composite (50 vol.% SiC fiber) over monolithic ceramic materials [Ref. 7].

The improvements in composite strength are achieved by a load transfer mechanism from the matrix to the fiber by means of interfacial shear stresses produced in the matrix on planes parallel to the fiber axis and in a direction parallel to the fiber axis. These interfacial shear stresses transfer the load from the weaker matrix to the much stronger reinforcing fibers. The composite fracture toughness can be a result of fiber-matrix debonding, fiber pullout, crack deflection, or crack impediment.

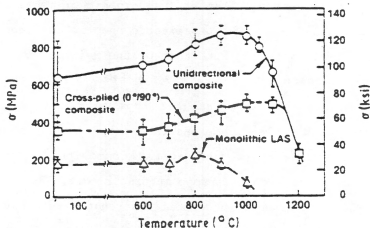


Figure 6. Flexural strength (3-point) of LAS-SiC yarn composites [Ref.7]

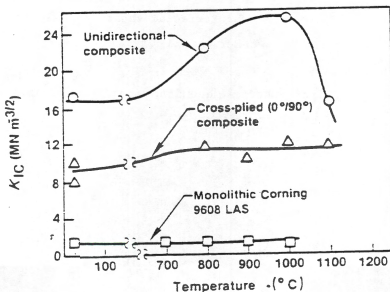
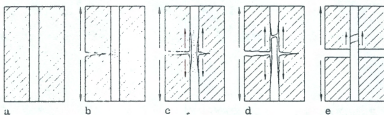


Figure 7. Fracture toughness  $K_{IC}$  of LAS-SiC yarn composites [Ref.7]

Figure 8 schematically details the process of crack impediment. The composite in its original state with frictional gripping of the fiber by the matrix is shown in (a); in (b) the crack in the matrix is stopped by the fiber, and in (c) the interfacial shear and lateral contraction of fiber and matrix results in debonding and crack deflection along the interface. Further debonding has taken place in (d) with the fiber beginning to fail, allowing the crack to bridge the fiber and continue through the matrix, and in (e) the crack has totally bridged the fiber and the broken fiber ends are pulled out against the frictional resistance of the interface. This process is responsible for the improved toughness that the SiC/LAS composites possess.



**Figure 8.** Crack impediment process in fiber-reinforced matrix [Ref.8]

It is accepted that the composite toughening mechanisms are dependent on the strength of the fiber/matrix interface [Ref. 8]. In the case where the interfacial strength or the

radial stresses imparted by the matrix on the fiber are too high, the composite strength increases. However it will behave elastically while fiber pullout will be prohibited and failure will be brittle in nature. On the other hand, if the interfacial shear strength is too low, then very little load transfer from the matrix to the fiber will occur, resulting in a much lower composite strength and improved toughness. Obviously an ideal composite will have an interface which is a compromise of the two cases.

The interface between the SiC fiber and LAS matrix has been reported to be an amorphous carbon rich layer approximately 70-170 nm wide [Ref. 9]. This carbon rich layer is formed during the composite fabrication process (hot pressing) from the chemical reaction:



The carbon layer itself has been observed to be 20-50 nm wide [Ref. 9]. This carbon layer on the surface of the fiber is crucial for the bonding strength between the fiber and the matrix.

#### B. FIBER/MATRIX INTERFACES

Extensive studies have been conducted on the fiber/matrix interface in hot-pressed fiber-reinforced glass-ceramic matrix composites. These studies have been carried out to develop an understanding of composite mechanical properties. Analysis completed to date have focused on the interface in the "as-received" composites, while little data



is available concerning the interfaces in composites exposed to oxidizing environments.

The fibers typically used in the composites are produced by melt-spinning of organic precursors (Nicalon). However, the fibers are unstable in elevated temperatures (greater than 1000 C). During the high temperature hot pressing procedure in the composite fabrication process, the unstable SiC fibers undergo oxidation at the fiber surface. This causes a microcrystalline graphitic carbon layer to form at the fiber/matrix interface, and also an amorphous SiO<sub>2</sub> layer forms on the surface of the fiber. The carbon rich layer results from the oxidation of the fiber by reaction (1) presented earlier and from the condensation of residual free carbon [Ref. 10]. Nicalon fibers typically have an increased carbon content near the fiber surface. The free carbon near the fiber surface has been found to promote an increase in the growth rate of the carbon layer at the interface, which is why the fibers are manufactured with carbon-rich stiochiometries. The kinetics of the layer formation are driven by the SiO<sub>2</sub> activity gradient across the interface [Ref. 10].

The formation of the carbon layer during composite fabrication is vitally important for the mechanical properties. It provides for the composite's improved toughness by facilitating the deflection of matrix cracks. The strengthening of the composite results from reinforcing the ceramic matrix with very strong fibers. The composite

toughness is enhanced when crack bridging occurs. This requires a debonding at the fiber/matrix interface, allowing cracks to bridge around the supporting fibers. The sliding resistance of the debonded interface governs the rate of load transfer from the matrix to the fiber. A small sliding resistance promotes higher composite toughness.

Experiments on SiC/LAS composites have shown that the carbon layer formed at the interface during fabrication readily debonds, promoting extensive fiber pullout. Composites heat treated in oxygen form an additional SiO<sub>2</sub> layer at the interface which becomes amorphous and does not readily debond, allowing crack extension through the fiber and a resultant decrease in toughness.[Ref. 12]

#### C. CORROSION OF SiC/LAS COMPOSITES BY Na<sub>2</sub>SO<sub>4</sub>

Many potential applications of silicon based glass-ceramics involve exposure to hot combustion gases, such as in hot section structural components of gas turbine engines shown in Figure 9. These structural components are subjected to a range of chemical attack processes depending on the temperature, pressure, and chemical composition of the operating environment.

It is well known that in a marine operating environment, airborne contaminants (containing sodium) can combine with sulfur impurities in the combustion gases to form sodium sulfate by the following chemical reaction:



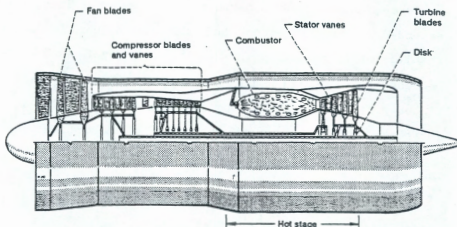


Figure 9. Schematic of gas turbine engine showing proposed structural applications for ceramics [Ref. 13]

Hot corrosion in the form of elevated temperature oxidation occurs when the condensed sodium sulfate is in the molten state, facilitating viscous flow and rapid diffusion through the glassy matrix.

Sodium sulfate is one of the most common deposits formed on structural components operated in a combustion gas atmosphere. Sodium sulfate is a highly stable, acidic salt. It is accepted that the deposit induced corrosion occurs in two steps: (1) the deposition of sodium sulfate, and (2) corrosive attack [Ref. 14]. Sodium sulfate is considered to be corrosive between its melting temperature (1157 K) and the dewpoint at which sodium sulfate deposits form. Although the region in which sodium sulfate becomes corrosive is somewhat limited, as shown in Figure 10, it can be very severe. Figure 10 also shows the dewpoint pressure dependence; as the

pressure increases, the dewpoint increases resulting in an expanded corrosive region [Ref. 13]. The higher temperature results in a diminished occurrence of  $\text{Na}_2\text{SO}_4$  deposition because the dewpoint temperature is exceeded. However, the higher pressures mean that the dewpoint temperature will also increase. This is an important consideration because future

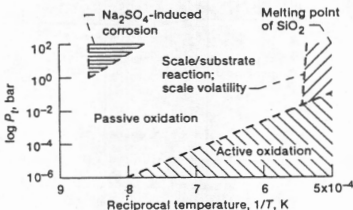
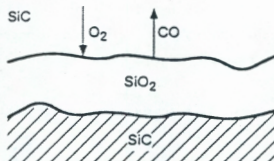


Figure 10. Types of corrosive attack as a function of reciprocal temperature [Ref. 13].

gas turbine engines will operate at higher temperatures and pressures, and knowing the engine operating parameters will be essential in determining whether  $\text{Na}_2\text{SO}_4$  deposits will form or not. The SiC reinforcing fibers are inherently unstable in atmospheric air and form a thin protective layer of silicon dioxide ( $\text{SiO}_2$ ) shown in Figure 11 [Ref. 13]. This protective layer is analogous to the  $\text{Al}_2\text{O}_3$  layer commonly found on aluminum alloys. The  $\text{SiO}_2$  layer has a very low

permeability to oxygen and thus serves as an effective oxidation barrier by restricting the flow of oxygen to the interface. The effectiveness of the layer is limited by its melting point (2000 K); when  $\text{SiO}_2$  is liquefied, the molecular transport and fiber oxidation rates increase dramatically.

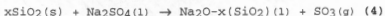


**Figure 11.** Schematic of  $\text{SiO}_2$  protective oxide scale formation on SiC fiber. [Ref. 13]

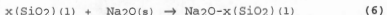
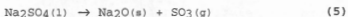
It is possible for the oxygen to get to the interface by either interstitial diffusion of molecular oxygen or the network exchange of ionic oxygen. Because the diffusion rate of molecular oxygen is roughly  $10^6$  times that of the ionic oxygen, the molecular transport by diffusion of oxygen through the  $\text{SiO}_2$  layer is the dominant operating mechanism. Additionally, at the elevated temperatures, the SiC fiber and  $\text{SiO}_2$  will react to form SiO and CO gas which generates gas pressure at the interface [Ref. 13].

It has been accepted that oxidation of the SiC fiber occurs by reaction (1) and can be broken down into five steps: (1) the transport of molecular oxygen gas to the SiO<sub>2</sub> surface, (2) diffusion of oxygen through the SiO<sub>2</sub> layer, (3) a reaction at the SiO<sub>2</sub>-SiC interface, (4) the transport of by-product gases back through the SiO<sub>2</sub> film, and (5) the transport of by-product gases from the surface. It is acknowledged that oxygen rather than the silicon is the mobile species during the oxidation process, thus the chemical reaction must take place at the SiO<sub>2</sub>-SiC interface. [Ref. 13]

The key chemical reactions in the hot corrosion of SiC by Na<sub>2</sub>SO<sub>4</sub> are:  $\text{SiC(s)} + 1.5\text{O}_2\text{(g)} \rightarrow \text{SiO}_2\text{(s)} + \text{CO(g)}$  (3)



The protective SiO<sub>2</sub> solid layer is transformed to a liquid scale which accelerates the corrosive attack due to increased transport through the liquid. Equation (4) can be rewritten in terms of the acid-base reactions:



SiO<sub>2</sub> is an acidic oxide and in accordance with the Lewis' concept of acid-base reaction, it reacts with the basic oxide Na<sub>2</sub>O forming the sodium silicate salt (Na<sub>2</sub>O-SiO<sub>2</sub>). The partial pressure of SO<sub>3</sub> (P<sub>SO<sub>3</sub></sub>) plays an important role in controlling the formation of sodium silicate salt. Na<sub>2</sub>SO<sub>4</sub> is a basic molten salt when it has a high activity of Na<sub>2</sub>O resulting from a low P<sub>SO<sub>3</sub></sub>. At higher P<sub>SO<sub>3</sub></sub>, Na<sub>2</sub>SO<sub>4</sub> is acidic

and does not react with the acidic  $\text{SiO}_2$  oxide. Jacobsen [Ref. 13] verified these predictions by treating test coupons in a burner rig using both low and high-sulfur fuels. More corrosion was observed on samples exposed to low-sulfur (low  $\text{P}_{\text{SO}_3}$ ) than those exposed to the high-sulfur fuels. Additionally, no sodium silicate was detected in the coupons exposed to the high-sulfur fuels.

Many types of the  $\text{SiC}$  fibers have excess carbon and non-homogeneous distribution through the fiber cross-section (Figure 12) which makes them highly susceptible to hot corrosion [Ref. 10 and 15]. Carbon tends to drive  $\text{Na}_2\text{SO}_4$  basic, such that even in conditions where  $\text{P}_{\text{SO}_3}$  is high enough to prevent the reaction between  $\text{Na}_2\text{SO}_4$  and  $\text{SiO}_2$ , corrosion can still be extensive. Oxygen partial pressure is another

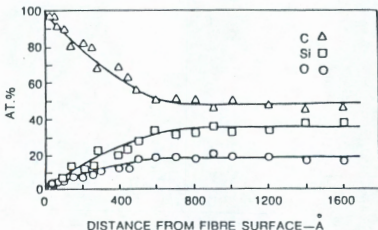


Figure 12. Plot of Carbon, Silicon, and Oxygen composition over the fiber cross-section. [Ref. 15]



factor that influences the hot corrosion process. It has been shown that high oxygen pressure drives  $\text{Na}_2\text{SO}_4$  acidic enough that dissolution of  $\text{SiO}_2$  does not occur. So, based on Lewis' concept of acid-base reactions alone, the hot corrosion regions of  $\text{Na}_2\text{SO}_4$  can be predicted.

Previous work by Wang, Kowalik, and Sands [Ref. 16] on sodium sulfate corrosion of LAS/ $\text{SiC}$  glass-ceramic composites demonstrated that hot corrosion by  $\text{Na}_2\text{SO}_4$  resulted in about 30% reduction in tensile strength of samples coated with the salt and heat-treated in air as shown in Figure 13. Wang, et al concluded that the presence of sodium sulfate in an oxidizing atmosphere resulted in rapid degradation of the  $\text{SiC}$  fibers and that the sodium reacted with the  $\text{SiO}_2$  and lowered its viscosity, which accelerated the diffusion rate of oxygen through the  $\text{SiO}_2$  layer.

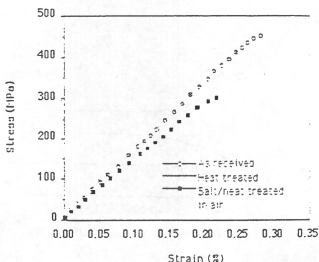


Figure 13. Stress-strain curves of LAS-SiC tensile specimens exposed to varying atmospheres [Ref. 16]

#### D. SEM AND XRD ANALYSIS OF SiC/LAS COMPOSITES

Previous work has been conducted by Maldia [Ref. 17] to characterize the chemical composition and morphology of as-received and annealed SiC/LAS composite samples. This work was accomplished by scanning electron microscopy (SEM) and x-ray diffractometer (XRD) analyses of the composite surface and cross-section. The samples examined by Maldia included as-received, annealed in argon, sodium sulfate coated and annealed in argon, annealed in oxygen, and sodium sulfate coated and annealed in oxygen. All heat treatments were performed at 900 C for 100 hours.

X-ray diffraction of the as-received sample indicated the presence of  $\beta$ -spodumene and mullite, with a large background from the glass. Small (three to five  $\mu\text{m}$ ) needle-like mullite laths and fine grained  $\beta$ -spodumene were noted in SEM backscattered electron micrographs, yet were too small for accurate EDS analysis.

The sample annealed in argon showed a dramatic decrease in the mullite content on the x-ray diffractogram. SEM micrographs also confirmed the disappearance of the needle-like mullite. The micrographs also revealed very little fiber degradation, except for those at the exposed surface.

SEM analysis of the sodium sulfate coated and annealed in oxygen sample indicated that severe fiber degradation had occurred. It was observed that the fibers near the surface were completely oxidized and significantly reduced in size. There also appeared to be a 100  $\mu\text{m}$  deep reaction layer where

the matrix and fibers had been attacked. XRD analysis indicated a significant decrease in mullite, while the dominant phase appeared to be  $\beta$ -spodumene, and a new phase Clineoenstatite ( $\text{MgO-SiO}_2$ ) had appeared. Large particles of  $\text{MgO-SiO}_2$  were observed in the SEM at the exposed surface near the degraded fibers. It was speculated that the presence of sodium silicate was responsible for the enhanced diffusion of MgO from within the matrix to the exposed surface, although no evidence of sodium in the corroded region was found.

SEM micrographs and x-ray diffractograms of the as-received, uncoated and annealed in argon, and sodium sulfate coated and annealed in oxygen samples are contained in Appendix A.

### III. SCOPE OF PRESENT WORK

The two principle methods available to characterize the structure and chemistry of the interfaces in ceramic matrix composites are the microanalysis of: (a) section surfaces in a scanning electron microscope (SEM), or (b) thin foils in a transmission electron microscope (TEM). The SEM rarely provides better than a 200 nm limit of resolution in backscattered (BS) electron imaging mode, largely due to the poor signal to noise ratio for atomic number contrast using BS electrons. Therefore, analysis of the interface requires the use of a TEM, where the limit of resolution can approach 0.3 nm for imaging and 2.0 nm for microchemical analysis. The improved resolution in the TEM is a result of the sample geometry, where there is nearly no bulb of interaction and a more defined excitation volume as shown in Figure 14.

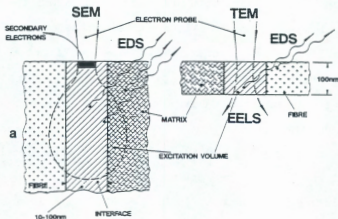


Figure 14 Schematic comparison of the electron beam excitation volume for SEM and TEM [Ref. 15]

Imaging of specimens in the TEM can be accomplished in bright field or dark field. For sufficiently thin sections, the electrons which enter the specimen at the top all emerge from the bottom. The path of these emerging electrons is altered by elastic and inelastic scattering. Placing a sufficiently small aperture in the back focal plane allows only the unscattered electrons which pass through the aperture to be seen in bright field images. Regions of the specimen which are thicker will scatter the electrons more and thus appear darker, this is called mass-thickness contrast. For crystalline specimens, an additional contrast mechanism is available to produce dark field images. This imaging technique, called diffraction contrast, can be used to clearly highlight a second phase which may be difficult to see in bright field. Dark field imaging can be accomplished in two ways. The first method involves displacing the aperture off of the optical axis and over the desired diffracted beam or ring. Alternatively, the primary electron beam can be tilted so that the desired diffracted beam (or ring) is traveling down the optical axis through a centered objective aperture. This method is useful for high resolution dark field imaging.[Ref. 18]

The chemistry of the interface can be obtained by either energy dispersive x-ray spectroscopy (EDS), or by electron energy loss spectroscopy (EELS). EDS is the most common analytical tool employed for interface characterization because of it's superior signal to noise ratio and convenient

use. However, EDS is limited by the window required to keep contamination from condensing on the cold detector. These windows are typically made up of a thin beryllium foil. This window absorbs a significant portion of the low energy x-rays, and therefore light elements ( $Z < 11$ ) are difficult to detect. The TEM used in this study is equipped with an ultra thin boron nitride window which allows for enhanced detection of lighter elements ( $Z \geq 6$ ).

With the macroscopic analysis of the composite samples already completed, the scope of the present work involved the microscopic analysis of SiC/LAS composite thin foils using the TEM and EDS equipped with an ultra thin boron nitride window. The emphasis of the study was placed on fiber/matrix interface morphology and chemistry since this has been identified as most important to the overall composite properties. Changes in the microstructural and chemical composition of the specimens were investigated. Selected area diffraction patterns, chemical composition obtained by EDS, and the x-ray diffractograms previously generated by Maldia [Ref. 17] were used to positively identify the crystalline phases present in the LAS matrix and to characterize the interfacial morphology.

#### IV. EXPERIMENTAL PROCEDURE

Each sample provided by the Naval Air Warfare Center consisted of three plies of continuous unidirectional Nicalon fibers hot-pressed in a lithium aluminosilicate matrix with a 90/0/90 fiber orientation. The matrix composition consisted of (wt%):  $\text{Li}_2\text{O}$ -3.2,  $\text{Al}_2\text{O}_3$ -20.0,  $\text{SiO}_2$ -67.5,  $\text{MgO}$ -2.5,  $\text{BaO}$ -1.2,  $\text{As}_2\text{O}_3$ -1.0,  $\text{B}_2\text{O}_3$ -3.1, and  $\text{ZrO}_2$ -1.5. The three samples examined were categorized as follows:

1. As-received.
2. No salt coating, heat treated at 900 C for 100 hours in flowing argon.
3. Coated with  $\text{Na}_2\text{SO}_4$  and heat treated at 900 C for 100 hours in flowing oxygen.

Sample (3) had an approximately  $3.0 \text{ mg/cm}^2$  salt coating prior to the heat treatment; this has been established to be roughly equivalent to the amount of  $\text{Na}_2\text{SO}_4$  deposited on gas turbine engine components operating at 900 C for 500 hours and a sulfur fuel impurity of 0.05% [Ref. 16]. The as-received sample provided the baseline for the chemical composition and interface morphology. Previous SEM analysis of samples heat treated in argon revealed a decrease in the mullite phase present, TEM examination of sample 2 was performed to verify these results and to determine the resulting effect on the chemical composition of the glass matrix.

#### A. THIN FOIL SAMPLE PREPARATION

A thin slice (approximately 250  $\mu\text{m}$ ) was cut from each sample using a Buehler Isomet Model 11-1180 Low Speed Saw and a 381  $\mu\text{m}$  thick diamond tip wafering blade. The slices were made in a direction parallel to the reinforcing fibers to provide the wafers with some rigidity. Thin foil samples made with diameters normal to fiber axis were too weak and broke apart during preparation. The thin wafer was then mechanically ground to a thickness of 100  $\mu\text{m}$  using a Gatan Model 623 Disc Grinder with 1000 grit and 2400 grit SiC paper. The heat treated samples were previously found to have an approximately 100  $\mu\text{m}$  thick reaction layer on the surface which was exposed to the environment during heat treatment. This required that the wafer be mechanically thinned from the interior side only in order to ensure that the thin foil analysis was being conducted inside the surface reaction layer. The sodium sulfate coated and annealed in oxygen sample was ground thin using ethanol as a lubricant instead of water, since sodium silicate is water soluble.

A three millimeter diameter disc (Figure 15) was then cut from the wafer on a VCR Group Model V7100 Precision Coring Tool. The disc was then mechanically dimpled with a Gatan Model 656 Precision Dimple Grinder on both sides leaving an approximately 20  $\mu\text{m}$  thick area in the center of the disc. The dimpled disc was then placed in a Gatan Model 600 Duomill ion milling machine (operated at 5 kV gun voltage) and was slowly thinned until a small perforation in



the center was detected. The perforated disc was then mounted into a dual tilt single stage holder for analysis in the TEM.

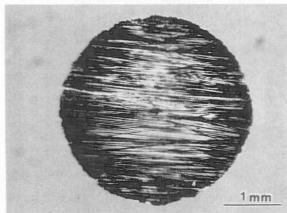


**Figure 15** Optical micrograph of 3 mm diameter disc after thinning to approximately 50  $\mu\text{m}$  showing the orientation of fibers (dark) within the matrix (light).

#### **B. TRANSMISSION ELECTRON MICROSCOPY**

A JEOL 100CX TEM was operated at 120 kV and conventional imaging, diffraction, and chemical micro-analysis of the fiber, interface, and the matrix were conducted using an ultra thin window equipped EDS. The spatial resolution of the electron beam (spot size 4) for EDS analysis was approximately 20 nm, which is smaller than the interface layer.

Selected area diffraction ring patterns from the  $\beta$ -SiC fiber were used to very accurately calibrate the camera length for later use in the analysis of crystalline phase zone axis patterns and ring patterns from other polycrystalline phases.

The thin foils were not glued to copper rings to prevent contamination during ion milling, (since microchemical analysis was to be performed) . Additionally, the thin foils were not covered with a carbon coating to enhance electrical conductivity because this would affect the microchemical analysis of the interfacial region where there was expected to be carbon from the fiber. The SiC fibers themselves possessed enough conductivity to minimize the charging effects for most analysis techniques employed.

## V. RESULTS AND DISCUSSION

### A. AS-RECEIVED SAMPLE

Examination of the as-received thin foil in the TEM revealed a matrix which was a mixture of glassy and crystalline regions. The crystalline phases (approximately 0.5 - 2.0  $\mu\text{m}$  grain size), identified to be  $\beta$ -spodumene and mullite (Figures 19-20), were evenly distributed throughout the glassy areas. The matrix was comprised of predominantly the crystalline phases. The regions immediately adjacent to the SiC fibers were found to be mostly glassy with some crystalline areas near the interface, as shown in Figure 16.

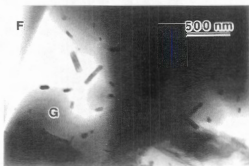


Figure 16. TEM bright field micrograph of the as-received sample with crystalline phases, glassy matrix (G), inclusions and a fiber(F)/matrix interface.

EDS analysis of the mullite and  $\beta$ -spodumene phases indicated that they were very close to stoichiometric ( $3\text{Al}_2\text{O}_3\text{-}2\text{SiO}_2$  and  $\text{LiO}_2\text{-Al}_2\text{O}_3\text{-}4\text{SiO}_2$  respectively) and the glass composition consisted of 88 wt%  $\text{SiO}_2$  and 12 wt%  $\text{Al}_2\text{O}_3$ . EDS spectrum for mullite is shown in Figure 17 and for  $\beta$ -spodumene in Figure 18. The mullite grain boundaries appeared much more distinctly than those for  $\beta$ -spodumene. Bright field TEM micrographs of the two crystalline phases clearly show the presence of dislocations, and selected area diffraction patterns were consistent with a fine grained crystalline material, as shown in Figures 19 and 20.

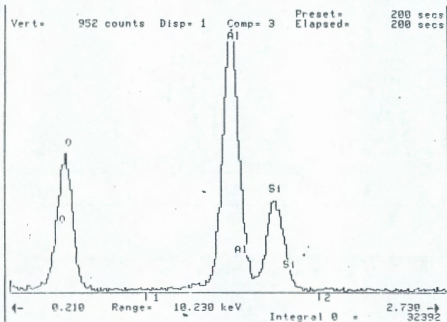


Figure 17. EDS spectra for mullite phase in the as-received sample.

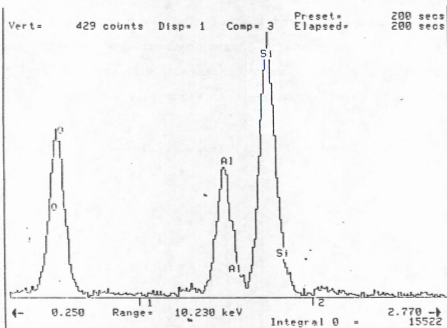
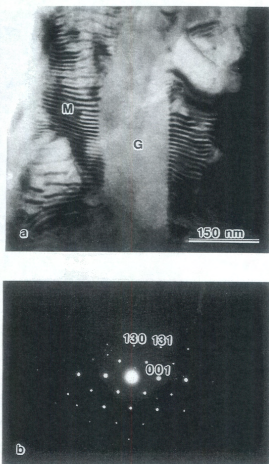
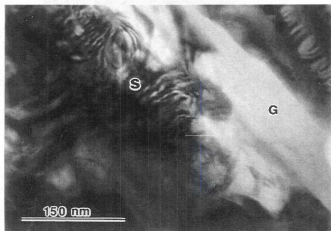


Figure 18. EDS spectra for  $\beta$ -spodumene phase in the as-received sample.



**Figure 19.** (a) TEM bright field micrograph of mullite phase (M) in glass (G), and (b) mullite [310] zone axis pattern. Note presence of extra spots due to double diffraction.



**Figure 20.** TEM bright field micrograph of  $\beta$ -spodumene phase (S) in glass matrix (G).

Small (50-100 nm) elongated  $\text{ZrO}_2$  and complexed  $\text{ZrO}_2\text{-MgO}$  particles (Figure 21) were found to be randomly distributed primarily in the glassy regions. The elongated  $\text{ZrO}_2$  particles were identified to be Baddeleyite, JCDPS diffraction file card no. 24-1165; a [110] zone axis pattern corresponding to Baddeleyite is shown in Figure 22.  $\text{ZrO}_2$  and MgO are commonly used as nucleating agents in glass-ceramics. The particles induce nucleation of crystalline structures during devitrification and enable a fine grain microstructure to be achieved.

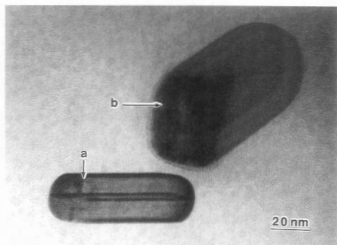


Figure 21. TEM bright field image of (a) Elongated  $\text{ZrO}_2$  and (b) complexed  $\text{ZrO}_2\text{-MgO}$  particles in glass matrix.

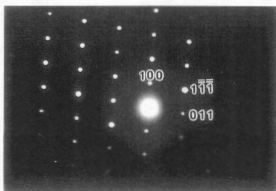
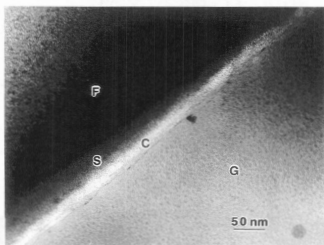


Figure 22.  $\text{ZrO}_2$  [110] Zone Axis Pattern



The fiber/matrix interface morphology consisted of two distinct layers between the SiC fiber and the LAS matrix. The layer closest to the fiber was identified with EDS to be amorphous SiO<sub>2</sub> and was typically 75-150 nm wide. This layer is lighter due to lack of diffraction contrast because it is amorphous. Figure 23 is a bright field image of a fiber/matrix interface clearly showing the lighter amorphous SiO<sub>2</sub> layer. The layer closest to the LAS matrix (brightest) was found to be graphitic carbon and approximately 20-50 nm wide. This layer is the brightest because of its low atomic number and would seem to be turbostratic with the basal planes aligned along the fiber axis as discussed by Kumar [Ref. 19].



**Figure 23.** Bright field image of fiber/matrix interface in the as-received sample. (F)=fiber, (G)=glass, (S)=SiO<sub>2</sub> layer, and (C)=graphitic carbon layer.

The graphitic carbon layer has previously been identified by Hsu and Speyer [Ref. 9] and Brennan [Ref. 10]. The layer is considered to have formed during the composite fabrication (hot pressing) and results from the chemical reaction:



This reaction has the lowest (most negative) free energy associated with all the chemical equilibria which describe the oxidation of SiC. The carbon layer is also thought to result from the condensation of carbon from within the fiber, which can be explained by the fact that the Nicalon fibers are not homogeneous in carbon content over their cross-section. The fibers tend to have more carbon at the outside of the fiber than inside in the as-formed condition. Figure 24 is a dark field image of an interface, taken from the 002 graphite reflection, with the light graphitic carbon layer shown clearly. Very fine  $\beta$ -SiC crystallites within the fiber can also be seen, this is because the displaced objective aperture is sufficiently large enough to overlap the 111  $\beta$ -SiC reflection. The silica ( $\text{SiO}_2$ ) formed during this reaction can diffuse into the LAS matrix, if the matrix is not locally silica rich [Ref. 10]. In the as-received sample, it was found that the glassy regions (silica rich) were predominantly adjacent to the interface. These glassy regions most likely acted as a diffusion barrier to the silica produced by the oxidation of the fiber, causing the pure silica layer to form at the fiber surface next to the

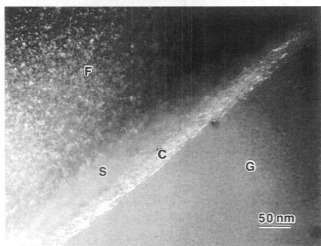


**Figure 24.** Dark field image of fiber/matrix interface in as-received sample, using the 002 graphite reflection. (F)=fiber, (G)=glass, (S)=SiO<sub>2</sub> layer, and (C)=graphitic carbon layer.

polycrystalline carbon layer of the interface, as shown in Figures 23 and 24. The smallest available selected area diffraction aperture was too large to isolate the individual layers of the interface alone, however, SAD patterns were obtained showing  $\beta$ -SiC rings and graphitic carbon rings superimposed on an amorphous SiO<sub>2</sub> background, shown in Figure 25.

The Nicalon fiber was found to be small  $\beta$ -SiC crystals in an amorphous silicon oxycarbide network with the latter being predominant at fiber surfaces near interfaces. The SAD ring pattern obtained from the fiber (Figure 26) shows the 111 primary reflection and 220 and 311 secondary reflections

characteristic of  $\beta$ -SiC, JCDPS diffraction card number 1-1119. The very fine (approximately 2-3 nm) crystals are difficult to see in the bright field image in Figure 27(a), however they appear very distinctly in a dark field image obtained from the 111  $\beta$ -SiC reflection and are shown in Figure 27(b). These results are very similar to that previously reported by Chaim and Heuer [Ref. 19] and also by Cooper and Chyung [Ref. 11].

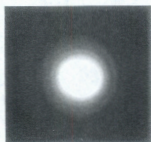


**Figure 25.** Selected area diffraction pattern from the interface and glassy matrix in the as-received sample showing rings corresponding to graphite superimposed on an amorphous background due to the  $\text{SiO}_2$ .

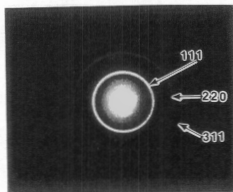
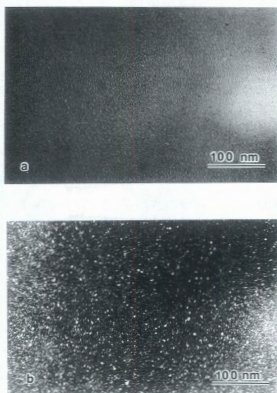


Figure 26. Selected area ring pattern from the Nicalon fiber in the as-received sample corresponding to  $\beta$ -SiC superimposed on amorphous silicon oxycarbide background.



**Figure 27.** (a) Bright field image of Nicalon fiber, (b) Dark field image of Nicalon fiber in as-received sample, using 111  $\beta$ -SiC reflection.

## B. NON-COATED, HEAT-TREATED IN ARGON SAMPLE

Examination of the non-coated, annealed in argon thin foil in the TEM revealed a matrix (within the reaction layer at the surface of the sample) which very closely resembled that of the as-received thin foil with, an apparent increase in glass content, a decrease in the amount of the mullite phase present, and the occasional presence of a new phase,  $\beta$ -eucryptite. The composition of the  $\beta$ -eucryptite phase was found to be very close to stoichiometric ( $\text{Li}_2\text{O}-\text{Al}_2\text{O}_3-2\text{SiO}_2$ ). Also noted along with the mullite decrease (which was clearly detected by x-ray diffraction as shown in Figure 28), was a concomitant increase in the alumina content of both the glass and  $\beta$ -spodumene. This behavior is consistent with a matrix approaching equilibrium, and was verified by examination of the LAS ternary phase diagram in Figure 1. The chemical composition of the glassy regions in this sample was found to be 84 wt%  $\text{SiO}_2$  and 16 wt%  $\text{Al}_2\text{O}_3$ .

The increased glass content was not expected with the annealing in argon. However, there is considerable oxygen in the Nicalon fibers which may possibly have diffused to and caused oxidation of the LAS matrix. Increased glass content would be expected for annealing in oxygen atmospheres as Kim and Moorhead [Ref. 21] have determined that the oxidation of an aluminosilicate matrix reinforced with  $\text{SiC}$  whiskers results in the formation of a non-protective aluminosilicate glass on the exposed surface. The increased glass content

seen in the TEM observations may also have been a function of location, where the thin area of the specimen may have been in a glassy-rich area of the sample.

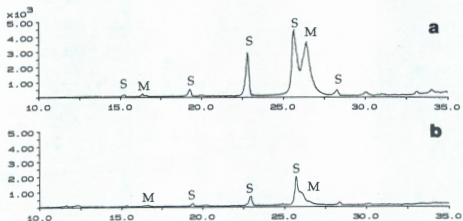


**Figure 28** Comparison of x-ray diffractograms from (a) as-received and (b) annealed in argon samples showing the decrease in mullite content [Ref. 17].

The presence of  $\beta$ -eucryptite (JCDPS card no. 26-840) was confirmed by comparing the x-ray diffractogram from the heat treated in argon sample to that the  $\beta$ -eucryptite, shown in Figure 29. The EDS spectrum (Figure 30) obtained from the thin foil sample also confirms the presence of  $\beta$ -eucryptite. These findings also confirm the previous SEM and XRD analysis indicating a decreasing mullite content.



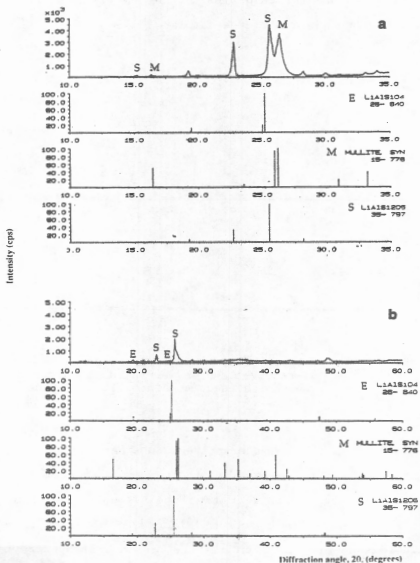


**Figure 29** Comparison of x-ray diffractograms from (a) as-received sample, and (b) the annealed in argon sample showing the presence of small  $\beta$ -eucryptite (E) peaks in the latter [Ref. 17].

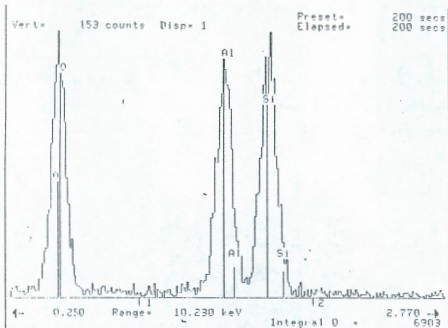


**Figure 30** EDS spectrum for  $\beta$ -eucryptite in the heat treated in argon sample.

### C. SALT COATED, HEAT-TREATED IN OXYGEN SAMPLE

Examination of the salt coated, annealed in oxygen thin foil in the TEM revealed a matrix which was a mixture of glass (88 wt%  $\text{SiO}_2$  and 12 wt%  $\text{Al}_2\text{O}_3$ ) and  $\beta$ -spodumene polycrystallites of 20 nm in diameter, shown in Figure 31. The microcrystalline phase was determined by selected area ring patterns to be  $\beta$ -spodumene with a chemical composition of 80 wt%  $\text{SiO}_2$  and 20 wt%  $\text{Al}_2\text{O}_3$ . The matrix was apparently a metastable mixture of glass and microcrystalline  $\beta$ -spodumene, shown in Figure 32(a) and (b), which is similar to the results obtained by Jewell, et al [Ref. 22] when they exposed a LAS glass to heat treatments at 950 and 1000 C.

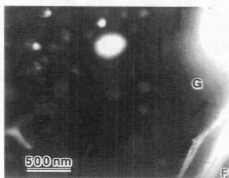
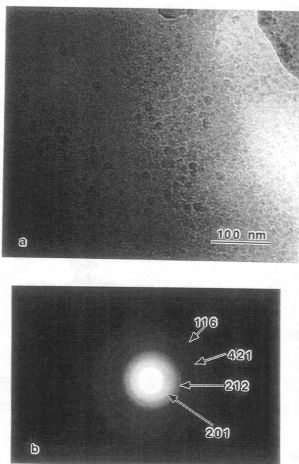


Figure 31 TEM bright field micrograph of the sodium sulfate coated and annealed in oxygen specimen. (G)=glass, (F)=fiber.



**Figure 32.** (a) Matrix prior to being irradiated with condensed electron beam, (b) SADP ring pattern from the matrix corresponding to  $\beta$ -spodumene crystallites.

When the electron beam was condensed onto the matrix, the apparently metastable matrix homogeneously recrystallized into small spherical crystallites (approximately 50-200 nm), as shown in Figures 33a and 33b. Although crystalline, the ring diffraction pattern associated with those particles was difficult to analyze as it was so faint. The chemical composition of the small grains was found to be 77 wt% SiO<sub>2</sub> and 23 wt% Al<sub>2</sub>O<sub>3</sub>; a comparison of this composition with the LAS ternary phase diagram suggests that the recrystallized region may be mullite or a polymorph of  $\beta$ -spodumene (Li<sub>2</sub>O-Al<sub>2</sub>O<sub>3</sub>-6SiO<sub>2</sub>), however it is not known which because the presence of lithium could not be detected by EDS. This behavior is similar to previous findings that metastable solid solutions with a structure analogous to  $\beta$ -quartz and having a chemical composition lying between the stoichiometric composition of  $\beta$ -eucryptite and SiO<sub>2</sub> are separated during crystallization of glasses between 800 and 900 C [Ref. 4]. Federer [Ref. 23] obtained similar XRD data from Na<sub>2</sub>SO<sub>4</sub> corrosion of SiC ceramics where the reaction layer was found to be amorphous and containing some tridymite and quartz, as suggested by Al<sub>2</sub>O<sub>3</sub>-SiO<sub>2</sub> binary phase diagram in Figure 34. However, the presence of both quartz and tridymite was not confirmed in the samples studied here.

The presence of sodium was not detected by EDS analysis, which suggests that the sodium sulfate was sufficiently acidic that sodium silicate did not form as a result of a reaction with either the LAS matrix or the fibers. This

suggests that the hot corrosion exposure in oxygen of the present work was equivalent to simulating a high sulfur fuel as discussed in section C of the background [Ref. 13].

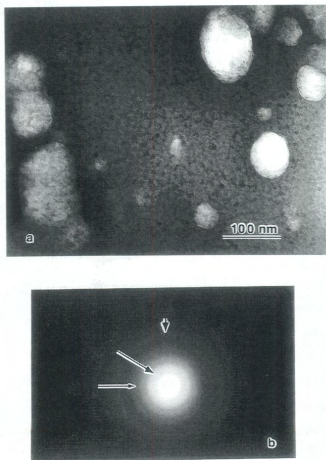


**Figure 33.** (a) Recrystallized matrix after being irradiated with condensed electron beam, (b) SADP ring pattern from recrystallized grains.

$\text{Al}_2\text{O}_3\text{-SiO}_2$

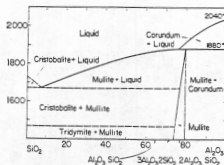
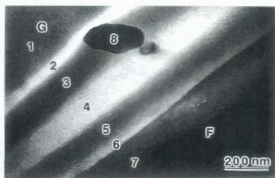


Figure 34. Binary  $\text{Al}_2\text{O}_3\text{-SiO}_2$  phase diagram [Ref. 4].

The most noteworthy finding in this sample was the development of a very large fiber/matrix interface. The interface had grown dramatically to nearly 600-800 nm in width due to the oxidation of the fiber, as shown in Figure 35. This interfacial layer is significantly smaller than those seen (1500-2000 nm) in the SEM micrograph of the exposed surface in Appendix A, because the thin foil specimen is actually located approximately further down from the exposed surface. In addition to the carbon rich and  $\text{SiO}_2$  layers previously identified in the as-received sample, the corroded sample had additional and larger carbon rich and  $\text{SiO}_2$  layers. EDS spectra obtained across the corroded interface in Figure 33 showed the layer closest to the matrix (position 2) to be carbon rich; while at position 3, the

carbon content decreases; and at position 4, the carbon content increases again; at position 5, the carbon content decreases; and finally at position 6 (next to the fiber), the carbon content increases again. Quantitative analysis from EDS spectra was not possible for the carbon content, therefore the previous comments of carbon rich and depleted regions were made by comparing relative peak heights for silicon, oxygen, and carbon from the EDS spectra. The  $\text{SiO}_2$  layers also contained small amount of aluminum, consistent with previous findings of Al diffusion during the oxidation of a SiC/LAS composite [Ref. 23]. The EDS spectra



**Figure 35.** TEM bright field image of a corroded fiber/matrix interface. (G)=glass, (F)=fiber, (S)= $\text{SiO}_2$  layer, (C)=graphitic carbon layer.



for each position across the corroded interface are contained in Appendix B. The alternating carbon rich and depleted layers can be readily seen in Figure 36 and Figure 37, which shows both bright and dark field TEM micrographs of a corroded interface. The dark field image was produced using the graphite 002 reflection, and the graphitic carbon is clearly seen as bright specks throughout the interfacial layers in the dark field micrograph, also seen are the  $\beta$ -SiC crystals in the fiber because the SADP aperture overlaps the 111  $\beta$ -SiC reflections. This type of layered structure has also been observed in an oxidized Nicalon SiC fiber-reinforced magnesium aluminosilicate composite by Kumar [Ref. 19] and its development is clearly a complex process depending on the local oxygen flux and partial pressure of oxygen across the interface.

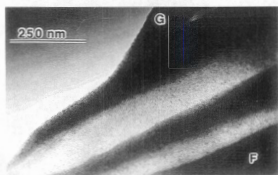


**Figure 36.** TEM bright field image of a corroded fiber/matrix interface. (G)=glass, (F)=fiber.

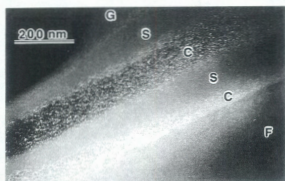


**Figure 37.** Dark field TEM micrograph of the corroded fiber/matrix interface from Figure 36, using the 002 graphite reflection. (G)=glass, (F)=fiber, (S)=SiO<sub>2</sub> layer, (C)=graphitic carbon layer.

The corroded interface morphology has been attributed to the marked change in mechanical properties of the SiC/LAS composite. Wang, et al. [Ref. 16] found that the ultimate failure strength of the corroded composite was reduced by thirty percent. Additionally, Bischoff, et al [Ref. 24] have noted a transition to a more brittle failure mode in the corroded composite. Bischoff, et al attribute the changes in mechanical properties to an abrupt increase in the sliding resistance between the fiber and matrix, yet there appears to be graphitic components within the interface which may allow sliding, as seen in Figures 35-37. Luh and Evans [Ref. 25] reported an increase in the interfacial shear strength of 20 times for a SiC/LAS composite heat treated in air at 1000 C. It was also found that the increase in interfacial shear

strength is dependent on environmental considerations since the same composite heat treated in an inert atmosphere did not exhibit the brittle failure as seen for the heat treated in oxygen composite. The increase in interfacial shear strength is also thought to be dependent on the matrix chemical composition, heat treatment temperature, and time of heat treatment [Ref. 24]. The transition of mechanical behavior of the heat treated composite can be described by a transition from notch-insensitive to notch-sensitive behavior [Ref. 25]. The presence of cracks in the matrix, may have a profound influence on the properties of the corroded composite since debonding does not occur, the cracks propagate through the fiber, resulting in the brittle behavior. Studies by Kagawa and Kurosawa [Ref. 26] have shown the LAS matrix to be susceptible to matrix microcracking along fiber axes for temperatures above 500 C due to thermal shock. The cracks were believed to primarily be the result of thermal expansion anisotropy in the a and c directions of the tetragonal  $\beta$ -spodumene. Matrix microcracks may also develop from the dissolution of mullite into glass, which involves volume changes that could impart sufficient residual stresses in the matrix to produce a crack.

The very small (50-100 nm)  $ZrO_2$  inclusions previously seen in the as-received sample had homogenized and grown very much larger (500-2000 nm), while still being evenly distributed throughout the matrix. The complexed  $ZrO_2$ -MgO inclusions seen in the as-received sample were not seen in

the corroded sample. This supports previous SEM findings that the Mg had diffused to the sample surface and formed Clineoestatite, which was clearly seen in the XRD diffractogram for the heat treated in oxygen sample shown in Appendix A.

## VI. CONCLUSIONS

Results of this study on the effects of sodium sulfate corrosion of SiC fiber-reinforced LAS glass-ceramic composites suggest the following:

- The SiC/LAS composite forms a graphitic (turbostratic) carbon rich layer at the fiber/matrix interface during fabrication, which is thought to be responsible for the excellent composite strength and toughness.
- SiC/LAS composites exposed to elevated temperatures in an argon atmosphere do not exhibit significant oxidation of the fiber except at the exposed surface, and the crystalline mullite phase dissolves leaving a surface reaction layer containing glass and  $\beta$ -spodumene richer in  $Al_2O_3$ .
- SiC/LAS composites exposed to elevated temperatures in an oxygen atmosphere, especially when coated with  $Na_2SO_4$ , experience significant fiber oxidation, the fiber/matrix interface transforms into alternating layers of graphitic carbon and amorphous  $SiO_2$ , and the matrix develops into a fine mixture of 20 nm grains of  $\beta$ -spodumene and glass.
- The amorphous  $SiO_2$  layer is thought to be responsible for the decrease in the composite strength experienced as a result of hot corrosion by sodium sulfate, because of an increase in the interfacial shear strength between the fiber and matrix.

- The morphology of the corroded interface suggests that the kinetics of the SiC fiber oxidation may be controlled by an oxygen diffusion mechanism and oxygen partial pressure gradient across the interface.
- The LAS matrix experienced severe hot corrosion by sodium sulfate which is responsible for its degraded mechanical properties. Therefore, this matrix material may not be ideally suited to applications in marine gas turbine engines.

## VII. RECOMMENDATIONS

It has been established that the fiber/matrix interface plays an important role in establishing the composite mechanical properties. It is for this reason that further research is needed to determine exactly the effect of the oxidation rate controlling factors and how they are influenced by fabrication variables. Additional research will require further TEM and microchemical analysis be performed on more corroded SiC/LAS composites. In particular, a comparison of the mechanical properties (tensile strength and toughness) for different composites which may contain additional layers on the fiber prior to fabrication, such as reaction/diffusion barriers and debond/shear layers. The composite studied in this work contained a  $B_2O_3$  (diffusion barrier) coating on the fiber prior to fabrication to help reduce fiber oxidation. A comparison with a similar composite without the fiber coating should be made to assess the effect of the coating.

The samples studied in this work were coated with a solid  $Na_2SO_4$  layer and then heat treated. This would simulate the condensation of sodium sulfate at low temperatures, followed by a reaction at elevated temperatures. This scenario describes one start-up, shut-down, and start-up cycle in a gas turbine engine. Most potential applications of gas turbine engines require many

such cycles. Thus, the heat treatment performed on these samples may not be indicative of the actual in-service conditions, particularly as the sodium sulfate dissolves as the heat treatment progresses.

Alternatively, the sodium sulfate may accumulate on engine components at higher temperatures above its dewpoint, in a similar fashion to that observed by Federer [Ref. 20]. This type of situation would be representative of salt deposit accumulation during actual engine operation. Therefore, some heat treatment cycles which take both of the deposit accumulation considerations into account are required to simulate actual in-service conditions to which the composite is likely to be exposed.



VIII. APPENDIX A

SEM MICROGRAPHS AND X-RAY DIFFRACTOGRAMS

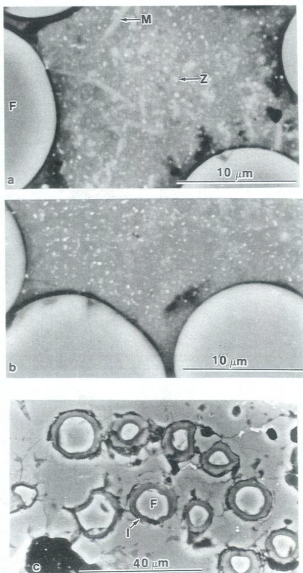


**Figure 38** SEM backscattered electron micrographs of (a) as-received sample, (b) noncoated and annealed in argon, and (c) Na<sub>2</sub>SO<sub>4</sub> coated and annealed in oxygen. (F)=fiber, (M)=mullite, (Z)=ZrO<sub>2</sub> particles, (I)=fiber/matrix interface.[Ref. 17].

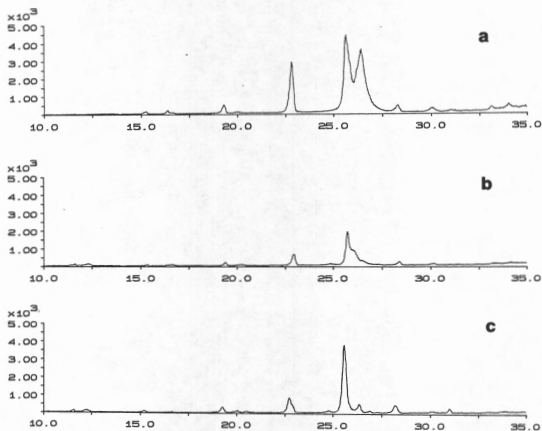


**Figure 39** X-ray diffractograms from (a) as-received, (b) noncoated and annealed in argon, and (c)  $\text{Na}_2\text{SO}_4$  coated and annealed in oxygen samples [Ref. 17].

IX. APPENDIX B  
CORRODED INTERFACE EDS SPECTRA

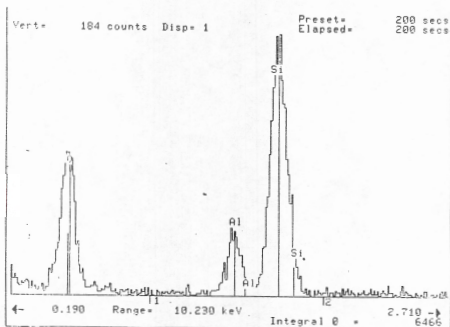
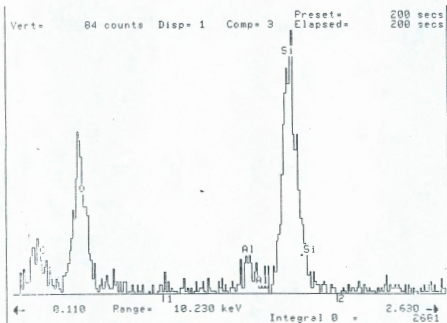
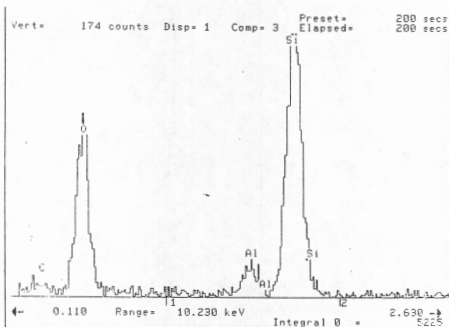


Figure 40 EDS spectrum corresponding to position 1 on the corroded fiber matrix interface shown in Figure 35.



**Figure 41** EDS spectrum corresponding to position 2 on the corroded fiber matrix interface shown in Figure 35.



**Figure 42** EDS spectrum corresponding to position 3 on the corroded fiber matrix interface shown in Figure 35.

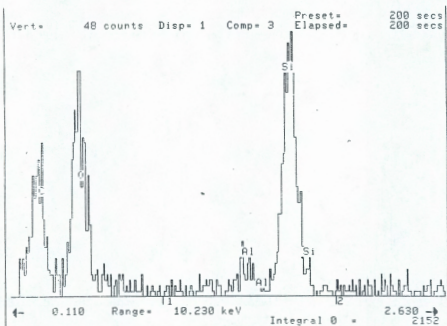


**Figure 43**

EDS spectrum corresponding to position 4 on the corroded fiber matrix interface shown in Figure 35.



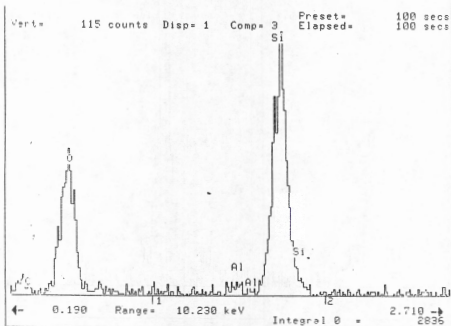


**Figure 44** EDS spectrum corresponding to position 5 on the corroded fiber matrix interface shown in Figure 35.

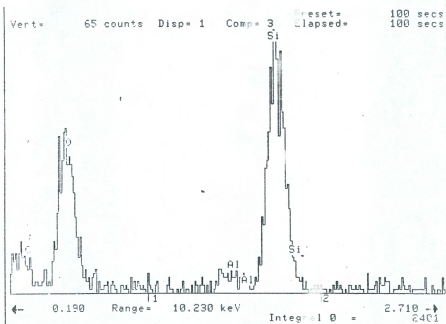


**Figure 45** EDS spectrum corresponding to position 6 on the corroded fiber matrix interface shown in Figure 35.

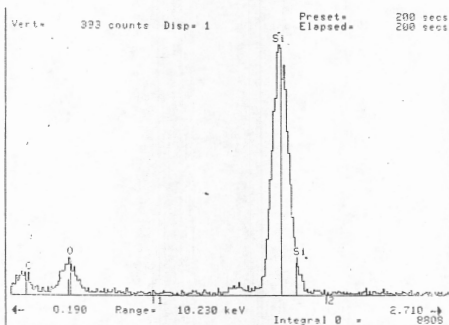
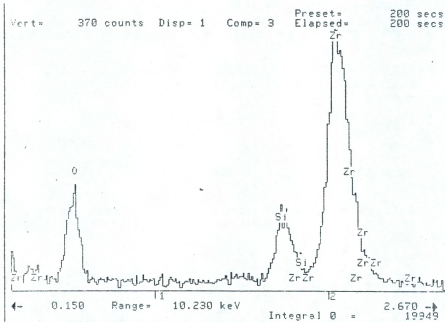


Figure 46 EDS spectrum corresponding to position 7 on the corroded fiber matrix interface shown in Figure 35.



**Figure 47** EDS spectrum corresponding to position 8 on the corroded fiber matrix interface shown in Figure 35.

# LIST OF REFERENCES

1. H. Scheidler and E. Rodek, "Li<sub>2</sub>O-Al<sub>2</sub>O<sub>3</sub>-SiO<sub>2</sub> Glass Ceramics," *Ceramic Bulletin*, Vol. 68, No. 11, p.1926-1930, 1989.
2. C. Cantalini and M. Pelino, "Characterization of Crystal Phases, Morphology, and Crystallization Processes in Lithium Aluminosilicate Glass-Ceramic," *Journal of Material Science*, 27(1992), 448-452.
3. D.R. Askeland, *The Science and Engineering of Materials*, PWS-Kent Publishing Co., 1989.
4. E.M. Levin, C.R. Robbins, and H.F. McMurdie, *Phase Diagrams for Ceramists*, Volume I, The American Ceramic Society, 1964.
5. Z. Strnad, *Glass Ceramic Materials*, Elsevier, 1986.
6. J. Hsu and R.F. Speyer, "Fabrication and Properties of SiC Fibre-Reinforced Li<sub>2</sub>O-Al<sub>2</sub>O<sub>3</sub>-6SiO<sub>2</sub> Glass-Ceramic Composites," *Journal of Material Science*, 27(1992) 381-390.
7. J.J. Brennan and K.M. Prew, "Silicon Carbide Fibre Reinforced Glass-Ceramic Matrix Composites Exhibiting High Strength and Toughness," *Journal of Material Science*, 17(1982) 2371-2383.
8. K.K. Chawla, *Composite Materials Science and Engineering*, Springer-Verlag, 1987.
9. J. Hsu and R.F. Speyer, "Interfacial Phenomenology of SiC Fibre Reinforced Li<sub>2</sub>-Al<sub>2</sub>O<sub>3</sub>-6SiO<sub>2</sub> Glass-Ceramic Composites," *Journal of Material Science*, 27(1992) 374-380.
10. J.J. Brennan, "SiC-Whisker-Reinforced Glass-Ceramic Composites: Interfaces and Properties," *Journal of American Ceramic Society*, 75[5] 1205-1216, 1992.
11. R.F. Cooper and K. Chyung, "Structure and Chemistry of Fibre-Matrix Interfaces in Silicon Carbide Fibre-Reinforced Glass-Ceramic Composites: An Electron Microscopy Study," *Journal of Material Science*, 22(1987) 3148-3160.

12. A.G. Evans and D.B. Marshall, "The Mechanical Behavior of Ceramic Matrix Composites," *Acta Metallurgica*, **37**(1989), 2567-2583.
13. N.S. Jacobson, "Corrosion of Silicon-Based Ceramics in Combustion Environments," *Journal of American Ceramic Society*, **76**(1) 3-28, 1993.
14. N.S. Jacobson, "Sodium Sulfate: Deposition and Dissolution of Silica," *Oxidation of Metals*, Vol.31, Nos. 1/2, 1989.
15. M.H. Lewis and V.S.R. Murthy, "Microstructural Characterisation of Interfaces in Fibre-Reinforced Ceramics," *Composites Science and Technology*, **42**(1991) 221-149.
16. S-W. Wang, R.W. Kowalik, and R. Sands, "Hot Corrosion of Two Nicalon Fiber Reinforced Glass Ceramic Matrix Composites," *Ceramic Engineering and Science Proceedings*, Vol. 14, No. 7-8, p.385-398, 1993.
17. L.C. Maldia, *Sodium Sulfate Corrosion of Silicon Carbide Fiber-Reinforced Lithium Aluminosilicate Glass-Ceramic Matrix Composites*, Master's Thesis, Naval Postgraduate School, Monterey, California, December, 1993.
18. P.J. Goodhew, and F.J. Humphreys, *Electron Microscopy and Analysis*, 2nd Edition, Taylor & Francis, 1988.
19. A. Kumar, *Microstructure-Property Relationships of SiC Fibre-Reinforced Magnesium Aluminosilicates*, PhD Thesis, University of Cambridge, U.K., 1994.
20. R. Chaim and A.H. Heuer, "The Interface Between (Nicalon) SiC Fibers and a Glass-Ceramic Matrix," *Advanced Ceramic Materials*, **2**(2) 154-158, 1987.
21. H-E. Kim and A.J. Moorhead, "Oxidation Behavior and Effects of Oxidation on the Strength of SiC-Whisker Reinforced Alumina," *Journal of Material Science*, **29**(1994) 1656-1661.
22. J.M. Jewell, et al, "Effect of Heat-Treatment Temperature on the Properties of Lithium Aluminosilicate Glass," *Journal of American Ceramic Society*, **74**(1) 92-97, 1991.
23. J.I. Federer, "Corrosion of SiC Ceramics by Na<sub>2</sub>SO<sub>4</sub>," *Advanced Ceramic Materials*, **3**(1), 56-61, 1988.

24. E. Bischoff, et al, "Microstructural Studies of the Interfacial Zone of a SiC-Fiber-Reinforced Lithium Aluminum Silicate Glass-Ceramic," *Journal of American Ceramic Society*, **72**[5] 741-745, 1989.
25. E.Y. Luh and A.G. Evans, "High-Temperature Mechanical Properties of a Ceramic Matrix Composite," *Journal of American Ceramic Society*, **70**[7], 466-469, (1989).
26. Y. Kagawa, N. Kurosawa, and T. Kishi, "Thermal Shock Resistance of SiC Fibre-Reinforced Borosilicate Glass and Lithium Aluminosilicate Matrix Composites," *Journal of Material Science*, **28**(1993), 735-741.

# INITIAL DISTRIBUTION LIST

- |    |   |   |
|----|---|---|
| 1. | Defense Technical Information Center<br>Cameron Station<br>Alexandria, VA 22304-6145  | 2 |
| 2. | Professor M.D. Kelleher, Code ME/Kk<br>Chairman<br>Department of Mechanical Engineering<br>Naval Postgraduate School<br>Monterey, CA 93943-5000 | 1 |
| 3. | Professor Alan G. Fox, Code ME/Fx<br>Mechanical Engineering Department<br>Naval Postgraduate School<br>Monterey, CA 93943-5000                  | 2 |
| 4. | Curricular Officer, Code 34<br>Department of Mechanical Engineering<br>Naval Postgraduate School<br>Monterey, CA 93943-5000                     | 1 |
| 5. | Dr. Shaio-Wen Wang<br>Code 6063<br>Aircraft Division<br>Naval Air Warfare Center<br>Warminster, PA 18794  | 1 |
| 6. | Library, Code 52<br>Naval Postgraduate School<br>Monterey, CA 93943-5000  | 1 |
| 7. | LT Richard K. Hunt, USCG<br>406 Sanford Drive<br>Fredericksburg, VA 22406   | 3 |



